Detection of Gamma Rays From a Starburst Galaxy

The H.E.S.S. Collaboration*

The full author list with affiliations can be found at the end of this paper

Starburst galaxies exhibit in their central regions a highly increased rate of supernovae, the remnants of which are thought to accelerate energetic cosmic rays up to energies of $\sim 10^{15}$ eV. We report the detection of gamma rays – tracers of such cosmic rays – from the starburst galaxy NGC 253 using the H.E.S.S. array of imaging atmospheric Cherenkov telescopes. The gamma-ray flux above 220 GeV is $F = (5.5 \pm 1.0_{\rm stat} \pm 2.8_{\rm sys}) \times 10^{-13}$ cm^{-2} s^{-1}, implying a cosmic-ray density about three orders of magnitude larger than that in the center of the Milky Way. The fraction of cosmic-ray energy channeled into gamma rays in this starburst environment is 5 times larger than that in our Galaxy.

Starburst galaxies are characterized by a boosted formation rate of massive stars and an increased rate of supernovae in localised regions, which also exhibit very high densities of gas and of radiation fields. Their optical and infrared luminosity is dominated by radiation from numerous young massive stars, most of which later explode as supernovae. Given that most cosmic rays in normal galaxies are expected to be accelerated in supernova remnants (*1*), starburst regions represent a favorable environment for the acceleration of cosmic rays, resulting in orders of magnitude higher cosmic ray energy densities compared to the local value in our galaxy [e.g. (*2*)]. Cosmic ray protons can produce gamma radiation by inelastic collisions with ambient gas particles and subsequent π^0-decay. Primary and secondary cosmic-ray electrons can also produce gamma radiation by Bremsstrahlung and up-scattering of low-energy photons from massive stars or from ambient radiation fields. Starburst galaxies are therefore considered promising sources of gamma-ray emission (*3, 4*). Here we report the detection of very high energy (VHE; $>$ 100 GeV) gamma rays from the starburst galaxy NGC 253.

NGC 253, at a distance of 2.6 to 3.9 Mpc (*5–7*), is one of the closest spiral galaxies outside of the Local Group. It is similar to our Milky Way in its overall star formation rate. Its nucleus, however, is a starburst region (*8*) of very small spatial extent (few 100 pc), characterised by a very high star formation rate per volume and thus also by a very large mechanical energy production in form of supernova explosions. Star formation activity is estimated to have been

*To whom correspondence should be addressed; E-mail: nedbal@ipnp.troja.mff.cuni.cz

going on for 20 – 30 million years (*8*) and can therefore be considered to be in a steady state for the time scales governing cosmic ray transport. A supernova rate of ~ 0.1 yr^{-1} has been inferred for the entire galaxy from radio (*9*) and infrared (*10*) observations. The rate is most pronounced in the central starburst region, where a conservative estimate yields a rate of supernovae ~ 0.03 yr^{-1}, which is comparable to that in our Galaxy (*8*). This suggests a very high local cosmic ray energy density. The mean density of the interstellar gas in the central starburst region is $n \simeq 600$ protons cm^{-3} (*11*), which is almost three orders of magnitude higher than the average density of the gas in the Milky Way. The thermal continuum emission of NGC 253 peaks in the far infrared (FIR) energy band at $\sim$100 μm with a luminosity that is ~ 5 times the total radiation from our own Galaxy (*12*). This FIR emission originates from interstellar dust, which reprocesses starlight from the numerous young massive stars. The emission is highly concentrated towards the small central starburst nucleus. Therefore, the density of the radiation field in the starburst region is about a factor 10^5 larger than the average value in the inner 100 pc around the Galactic Center. The activity of NGC 253 has been shown to be of a pure starburst nature and not due to an active supermassive black hole (*13,14*). Observations of radio (*15,16*) and thermal X-ray emission (*17,18*) show a hot diffuse halo, consistent with the existence of a galactic wind extending out to ~ 9 kpc from the galactic plane that transports matter and cosmic rays from the nucleus to inter-galactic space and reaches asymptotically a bulk speed of $\sim$ 900 km/s (*19*).

Given its proximity and its extraordinary properties, NGC 253 was predicted to emit gamma rays at a detectable level (*4*). Recent calculations give similar results (*21, 22*). Previously, only upper limits have been reported in the gamma-ray range, in the MeV-GeV range by EGRET (*20*), and in the TeV range by H.E.S.S. [based on 28 hours of observation (*23*)] and by CANGAROO III (*24*). We report the result of continued observations of NGC 253 with the H.E.S.S. telescope system with a much larger data sample. (See the Supporting Online Material (SOM) for a description of the experiment and the detection technique.)

We obtained observations in 2005, 2007 and 2008. After rejecting those data that did not have the required quality, we analyzed 119 hours of live-time data . Even with this extremely long exposure, the measured VHE gamma-ray flux of NGC 253 is at the limit of the H.E.S.S. sensitivity. Thus advanced image analysis techniques were required to extract a significant signal on top of the uniform background of local cosmic rays impinging on the Earth's atmosphere – only one out of 10^5 recorded air showers represents a gamma-ray from NGC 253. We used the "Model Analysis" technique (*25*) (SOM), based on which we detected an excess of 247 events from the direction of NGC 253 above 220 GeV, corresponding to a statistical significance of 5.2 standard deviations (Fig. 1). The signal is steady and stable (a fit over the period of three years to a constant has a chance probability of 47%). The source position is $\alpha_{J2000} = 0^{\rm h}47^{\rm m}33^{\rm s}.6 \pm 30^{\rm s}$, $\delta_{J2000} = -25^\circ 18' 8'' \pm 27''$ consistent with the position of the optical center of NGC 253 ($\alpha_{J2000} = 0^{\rm h}47^{\rm m}33^{\rm s}.1$, $\delta_{J2000} = -25^\circ 17' 18''$). The distribution of excess events is consistent with the point spread function of the H.E.S.S. instrument, implying a source size of less than $4.2'$ (at a 1σ confidence level, see Fig. 2 for a comparison of the angular distribution of the gamma events with a point-like simulated signal). The integral flux of the

source above the threshold of 220 GeV is $F(> 220\,\mathrm{GeV}) = (5.5 \pm 1.0_{\mathrm{stat}} \pm 2.8_{\mathrm{sys}}) \times 10^{-13}$ cm^{-2} s^{-1}. This corresponds to 0.3 % of the VHE gamma-ray flux from the Crab Nebula (*29*); given the well-known uncertainties in the diffusion part of the particle transport properties as well as the only approximate knowledge of the starburst parameters, it is consistent with the original prediction (*4*) (Fig. 3).

As an external galaxy detected in gamma rays which, as a key property, does not contain a significant active galactic nucleus, NGC 253 is a member of a class of gamma-ray emitters external to the Milky Way and the associated Large Magellanic Cloud (LMC). These gamma-ray emitters apparently produce their own cosmic ray population. Except for the starburst, NGC 253 is a normal galaxy. So far only the LMC, a small and close satellite of the Milky Way, was detected in gamma rays with the EGRET instrument (*30*). In contrast there exists a class of external galaxies detected in gamma-rays whose emission is – according to present knowledge – exclusively due to an active galactic nucleus (AGN), driven by a supermassive Black Hole in their center. Their physical characteristics are quite distinct from normal galaxies and not the subject of the discussion here.

The detection of NGC 253 in VHE gamma rays implies a high energy density of cosmic rays in this system. One can calculate a corresponding cosmic ray density directly from the H.E.S.S. observations. Assuming a dominant hadronic origin of the gamma-ray emission, the spatial density $N_{\mathrm{p}}(> E_{\mathrm{p}})$ of the gamma-ray generating protons in the starburst region with an energy exceeding $E_{\mathrm{p}} \approx 220/0.17\ \mathrm{GeV} \approx 1300$ GeV is about 4.9×10^{-12} cm^{-3} for the measured gamma-ray flux above 220 GeV, independent of the distance to NGC 253. This is about 2000 times larger than the corresponding Galactic cosmic ray number density at the Solar System. And it is about 1400 times higher than the density at the center of our Galaxy (*31*). Taking $E_{\mathrm{p}} N_{\mathrm{p}}(> E_{\mathrm{p}})$ as a rough measure of the energy density of cosmic rays above energy E_{p} in NGC 253, $E_{\mathrm{p}} N_{\mathrm{p}}(> E_{\mathrm{p}}) \approx 6.4$ eV cm^{-3} for $E_{\mathrm{p}} > 1300$ GeV. This is larger than the entire cosmic-ray energy density in the Galaxy near the Solar System which is dominated by GeV-particles.

Gamma-ray production represents one channel for conversion and loss of cosmic rays at TeV energies. The time between inelastic collisions of hadronic cosmic rays and target protons and nuclei at $E_{\mathrm{p}} \approx 1300$ GeV is of the order of $10^5\,\mathrm{yr}$ for a mean gas density of about 600 protons cm^{-3}. These collisional losses compete with two other processes in starbursts: spatial losses of particles convected out of the considered region by the wind, and diffusive losses (see the SOM for a summary of the cosmic-ray transport characteristics in NGC 253). Because of the very high gas density in the nucleus of NGC 253, the ratio of hadronic gamma-ray production to energy loss by transport is considerably higher than for a galaxy like ours. In the Milky Way, the $\sim$ 1300 GeV gamma-ray generating charged particles encounter about 0.6 g cm^{-2} of matter before they escape, extrapolating results from (*32*). Their mean free path for inelastic nuclear collisions is equivalent to about 56 g cm^{-2}. Therefore, the Galactic ratio of gamma-ray production probability to the escape probability of 1300 GeV particles is about 10^{-2}. If the cosmic-ray energy production in the starburst region of NGC 253 is in equilibrium with losses caused by nuclear collisions, then, for the measured gas density and supernova rate – together

with an assumed cosmic-ray production efficiency of 10^{50} erg per event and a production spectrum $\propto E^{-2.1}$ (*3,23*) – the expected integral gamma-ray flux above 220 GeV would be $\approx 10^{-11}$ cm^{-2} s^{-1}. The observed flux is smaller than this calorimetric flux by a factor $\approx 5 \times 10^{-2}$ – again independent of the distance. Therefore, the starburst region is only mildly calorimetric. For a comparison see (*23,33*). Nevertheless, the numbers imply that the conversion efficiency of protons into gamma rays in the starburst region of NGC 253 exceeds that in our Galaxy by almost an order of magnitude. This comparatively high efficiency has another consequence: assuming that the remaining structure of NGC 253 is approximately the same as in our Galaxy, then the starburst nucleus is about 5 times brighter in VHE gamma-rays than the associated galaxy, and the starburst nucleus should outshine the rest of NGC 253. This is consistent with the detection of a H.E.S.S. point source (Fig. 1).

Given these results one may ask whether they have a wider significance regarding the non-thermal particle population in the Universe. A starburst galaxy such as NGC 253 is a potential model for a phase of galaxy formation as well as for two-body galaxy-galaxy interactions, especially in the dense environment of large galaxy clusters. High-energy gamma-ray emission as a result of these processes should accompany the thermal IR emission of such luminous Infrared Galaxies. The galactic winds present in these systems are expected to massively populate intergalactic space with nucleosynthesis products and cosmic rays.

Acknowledgements: The support of the Namibian authorities and of the University of Namibia in facilitating the construction and operation of H.E.S.S. is gratefully acknowledged, as is the support by the German Ministry for Education and Research (BMBF), the Max Planck Society, the French Ministry for Research, the CNRS-IN2P3 and the Astroparticle Interdisciplinary Programme of the CNRS, the U.K. Science and Technology Facilities Council (STFC), the IPNP of the Charles University, the Polish Ministry of Science and Higher Education, the South African Department of Science and Technology and National Research Foundation, and by the University of Namibia. We appreciate the excellent work of the technical support staff in Berlin, Durham, Hamburg, Heidelberg, Palaiseau, Paris, Saclay, and in Namibia in the construction and operation of the equipment.

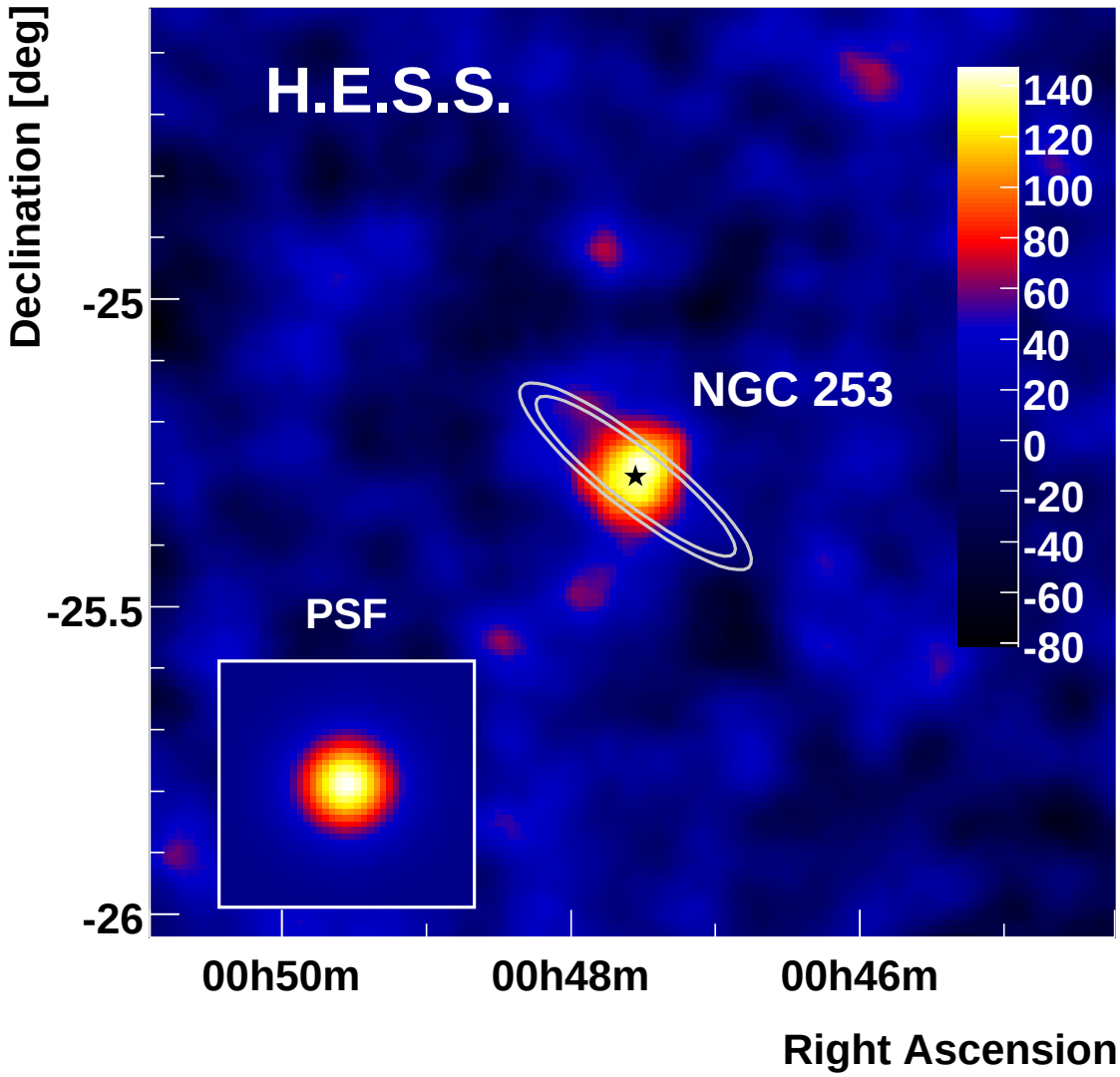

Fig. 1. A smoothed map of VHE gamma-ray excess of the $1.5^\circ \times 1.5^\circ$ region around NGC 253. A Gaussian with RMS of $4.2'$ was used to smooth the map in order to reduce the effect of fluctuations. The star shows the optical center of NGC 253. The inlay represents an image of a Monte Carlo simulated point source (i.e. the point-spread function of the instrument). The white contours represent the optical emission of the whole NGC 253, demonstrating that the VHE emission originates in the nucleus and not in the disk. The contours correspond to constant surface brightness of 25 mag. arcsec.$^{-2}$ – traditionally used to illustrate the extent of the optical galaxy – and 23.94 mag. arcsec.$^{-2}$ as given by fits of (*34*).

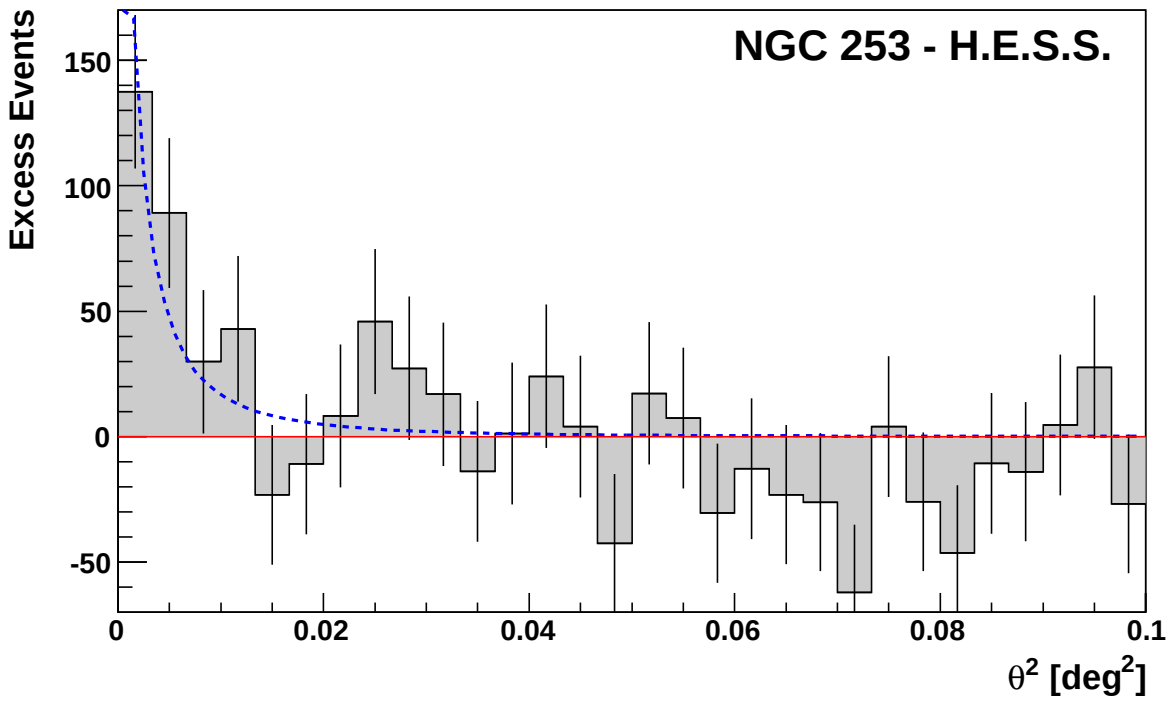

Fig. 2. Reconstructed directions of the gamma-ray like events around NGC 253. θ denotes the angular distance between the arrival direction and the position of the object. The background estimated from off source regions, is uniform in the θ^2 representation and has been subtracted here. The signal is consistent with a H.E.S.S. point source (blue dashed line) corresponding to $\theta < 4.2'$ or < 3.2 kpc at a distance of 2.6 Mpc.

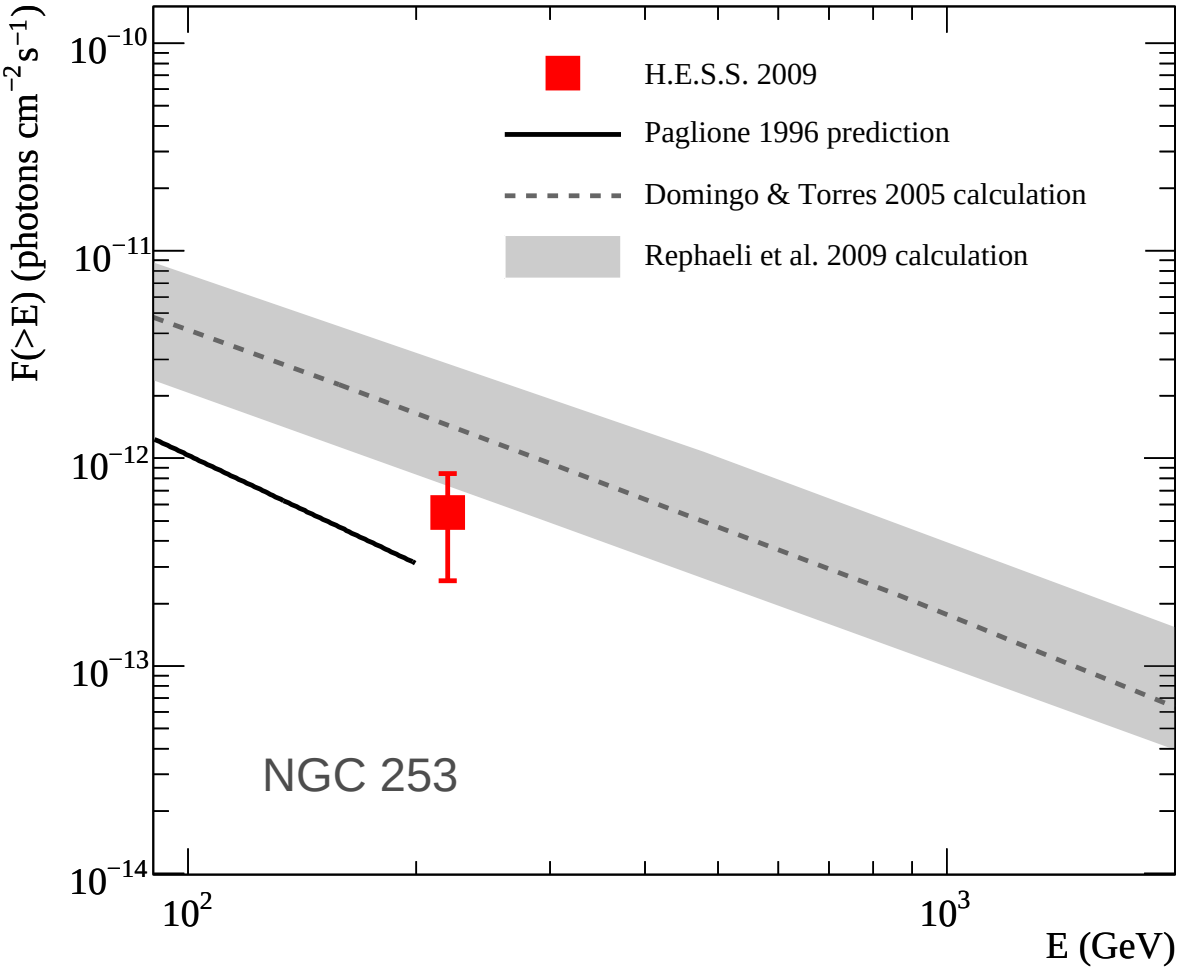

Fig. 3. The observed integral flux of gamma rays from NGC 253 (red point) is compared to theoretical estimates (*4*,*21*,*23*). The solid line corresponds to the prediction by (*4*). The dashed line corresponds to the model (*21*). The grey-shaded band denotes the estimate (*22*). The error of the H.E.S.S. measurement includes systematic errors.

References and Notes

1. Aharonian, F. A., *et al.*, *Nature*, **432**, 75 (2004)
2. Völk, H. J., Klein, U. and Wielebinski, R., *Astron. Astrophys.*, **213**, L12 (1989)
3. Völk, H. J., Aharonian, F. A. and Breitschwerdt, D., *Space Sci. Rev.*, **75**, 279 (1996)
4. Paglione, T. A. D., Marscher, A. P., Jackson, J. M. & Bertsch, D. L., *Astrophys. J.*, **460**, 295 (1996)
5. Puche, D., & Carignan, C., *Astron. J.*, **95**, 1025 (1988)
6. Rekola, R., Richer, M. G., McCall, M. L., Valtonen, M. J., Kotilainen, J. K., & Flynn, C., *Mon. Not. R. Astron. Soc.*, **361**, 330 (2005)
7. The following description is based on a distance of 2.6 Mpc, the final conclusions are, however, independent of distance.
8. Engelbracht, C. W., Rieke, M. J., Rieke, G. H., Kelly, D. M., & Achtermann, J. M., *Astrophys. J.*, **505**, 639 (1998)
9. Antonucci, R. R. J. and Ulvestad, J. S., *Astrophys. J.*, **330**, L97 (1988)
10. van Buren, D., & Greenhouse, M. A., *Astrophys. J.*, **431**, 640 (1994)
11. Sorai, K., Nakai, N., Kuno, N., Nishiyama, K., & Hasegawa, T., *Publ. Astron. Soc. Jpn.*, **52**, 785 (2000)
12. Rice, W., Lonsdale, C. J., Soifer, B. T., *et al.*, *Astrophys. J. Suppl. Ser.*, **68**, 91 (1988)
13. Brunthaler, A., Castangia, P., Tarchi, A., *et al.*, *Astron. Astrophys.*, **497**, 103 (2009)
14. Bauer, M., Pietsch, W., Trinchieri, G., *et al.*, *Astron. Astrophys.*, **467**, 979 (2007)
15. Carilli, C. L., Holdaway, M. A., Ho, P. T. P., & de Pree, C. G., *Astrophys. J.*, **399**, L59 (1992)
16. Heesen, V., Beck, R., Krause, M., & Dettmar, R.-J. *Astron. Astrophys.*, **494**, 563 (2009)
17. Dahlem, M., Weaver, K. A., & Heckman, T. M. 1998, *Astrophys. J. Suppl. Ser.*, **118**, 401 (1998)
18. Bauer, M., Pietsch, W., Trinchieri, G. *et al.*, *Astron. Astrophys.*, **489**, 1029 (2008)
19. Zirakashvili, V. N., Völk, H. J., *Astrophys. J.*, **636**, 140 (2006)
20. Blom, J. J., Paglione, T. A. D., & Carramiñana, A., *Astrophys. J.*, **516**, 744 (1999)

21. Domingo-Santamaría, E., & Torres, D. F., *Astron. Astrophys.*, **444**, 403 (2005)

22. Rephaeli, Y., Arieli, Y. & Persic, M., *Mon. Not. R. Astron. Soc.*, submitted, (available at http://arXiv.org/abs/0906.1921)

23. Aharonian, F. *et al. (H.E.S.S. Collaboration), Astron. Astrophys.*, **442**, 177 (2005)

24. Itoh, C., *et al. (CANGAROO Collaboration), Astron. Astrophys.*, **462**, 67 (2007)

25. The "Model Analysis" is based on a comparison and fit of observed air shower images with a pre-computed library of images (*26*); Another analysis technique, based on a machine learning algorithm called Boosted Decision Trees (BDT) (*27*), was used to verify the results. It was trained with simulated gamma-rays and with real cosmic-ray data from background fields (*28*). Both algorithms yield an improvement by a factor 1.5 to 1.7 in the statistical significance of faint sources compared to the standard image analysis (*29*), as verified with a number of other gamma-ray sources. The "Model Analysis" result is found to be consistent with the one obtained with the "BDT" analysis. Details are given in the SOM.

26. de Naurois, M., Rolland, L., *Astroparticle Physics*, accepted for publication, (available at http://arXiv.org/abs/0907.2610)

27. Breiman, L., Friedman, J., Stone, C.J., and Olshen, R.A., *Classification and Regression Trees* (Wadsworth, Stamford, 1984)

28. Ohm, S., van Eldik, C., & Egberts, K., *Astroparticle Physics*, **31**, 383-391 (2009)

29. Aharonian, F. *et al. (H.E.S.S. Collaboration), Astron. Astrophys.*, **457**, 899 (2006)

30. Sreekumar, P., Bertsch, L.D., Dingues, B. L. *et al.*, *Astrophys. J.*, **400**, L67 (1992)

31. Aharonian, F., *et al. (H.E.S.S. Collaboration), Nature*, **439**, 695 (2006)

32. Swordy, S.P., Müller, D., Meyer, P., LḤeureux, J., & Grunsfeld, J. M., *Astrophys. J.*, **349**, 625 (1990)

33. Thompson, T.A., Quataert, E., Waxman, E., *Astrophys. J.*, **645**, 219 (2007)

34. Pence, W. D., *Astrophys. J.*, **239**, 54 (1980)

Supporting Online Material

www.sciencemag.org
Materials and Methods
Supporting text
Figs. S1, S2
References

Supporting Online Material

Detection technique

H.E.S.S. is an array of four imaging atmospheric Cherenkov telescopes (IACTs) located in the Khomas highlands in Namibia [see (*S1*) for a detailed description of the system]. IACTs observe the Cherenkov light produced by relativistic particles in electromagnetic showers resulting from gamma-ray collisions in the atmosphere, thus using the Earth's atmosphere as a detector medium. The optical Cherenkov light is detected with an ultra-fast optical camera assembled from photomultiplier pixels that takes images of the showers. Gamma rays are separated from the charged cosmic rays on the basis of different shower properties [e.g. (*S2*)]. H.E.S.S. observes the sky in the VHE gamma-ray regime. With the standard analysis it can detect a source of 1% of the flux of the "standard candle" Crab Nebula in 25 hours at a 5σ level (*S3*).

Data set and data quality

The large dataset together with the weak signal of NGC 253 require careful control of the quality of the data used for analysis. In order to reduce the effect of hardware problems and atmospheric fluctuations on the flux determination, a system of quality criteria cuts is applied to reject the data with bad or dubious quality [see also discussion in (*S3*)].

A substantial part of the systematic error of the flux is caused by atmospheric conditions. Cloudy sky and dust in the atmosphere absorb the Cherenkov light from the electromagnetic shower, which results in a lower detection rate and in an underestimation of the flux. The rate at which cosmic-ray showers trigger the instruments provides a sensitive monitor for atmospheric transparency. As a function of the zenith angle of telescope pointing, a nominal trigger rate is estimated for each 28-minute observation run. If the real trigger rate is less than 80% of the predicted value, the run is rejected. Additionally, to avoid intra-run fluctuations caused by e.g. clouds, a cut on the RMS of the trigger rate within one run is applied (max. 10% is allowed). Further cuts detailed by (*S3*) are applied in order to limit the effect of malfunctioning pixels in the camera and the correct pointing and tracking of the telescopes as well as to assure a proper calibration of each run.

NGC 253 was observed with the full array of four H.E.S.S. telescopes during 2005, 2007 and 2008 for a total of 192 hours. After applying the quality selection cuts and correcting for the instrument dead-time, 119 hours of good-quality live-time data is used for the analysis. The average zenith angle of these observations was 11° resulting in an energy threshold of 220 GeV for the "Model analysis" and 260 GeV for the BDT analysis, after all cuts applied in the respective analyses.

"Model" image analysis

The main results presented here were produced with the *Model Analysis* (*S4*). Conventional analysis techniques rely on an image cleaning procedure to extract relevant information in the camera, and reduce the shower information to a few parameters through a parametrization of the image shape. In contrast, the Model Analysis is based on a pixel-per-pixel comparison of the actual recorded intensity of a signal in the camera with a pre-calculated shower model, without any image cleaning or parametrization. The shower model is based on a semi-analytical description of shower development in the atmosphere. Template images for a large range in primary energy, zenith angle, impact distance and depth of first interaction are generated using a dedicated code, stored into files, and used in the comparison with the actual images. The noise distributions in the pixel due to the night sky background is taken into account in the model fit. A precise description of statistical fluctuations is used in form of a log-likelihood minimization, which results in a superior treatment of shower tails. Therefore, the Model Analysis results in a more precise reconstruction and a better background suppression than more conventional techniques, thus leading to an improved sensitivity. The remaining background in either method is estimated using reflected control regions (*S3*).

A goodness-of-fit approach is chosen to compare the model prediction and the actual shower images, in order to check the compatibility of the recorded events with a pure gamma-ray hypothesis and therefore provide gamma-hadron separation. The goodness-of-fit is defined as a normalised sum over all pixels of the difference between the actual pixel log-likelihood (at the end of minimization) and its expectation value, taking into account Poisson fluctuations of the number of photons, electronic and night sky background fluctuations. The goodness-of-fit parameter retains 70% of gamma-rays and rejects more than 95% of background events, yielding a quality factor

$$Q = \frac{\epsilon_\gamma}{\sqrt{\epsilon_{\mathrm{hadrons}}}} \approx 4 \tag{1}$$

Additional discriminating parameters, such as the depth of first interaction, are also used in the Model Analysis to improve the gamma-hadron separation. Cross-checks performed on several sources (Crab Nebula, PKS 2155-305, and others) show that, on average, the Model Analysis yields a gamma-ray efficiency in the order of 2.5 times higher than that of the Hillas reconstruction method with hard cuts (used in most H.E.S.S. publications), with a similar increase in the background level (depending in particular on the source spectral index). The corresponding improvement of sensitivity is by a factor of slightly less than 2.

Analysis using Boosted Decision Trees

The results were cross-checked using an analysis based on an independent calibration procedure and a different background discrimination method. It is based on a machine learning algorithm called Boosted Decision Trees (BDT) (*S5,S6*). This mathematical tool was also utilized for particle identification in high-energy physics [e.g. (*S7,S8*)] and was applied recently in astrophysics

for e.g. supernova searches (*S9*). A similar approach called Random Forest (*S10*), which is also based on decision trees, was utilized in ground-based VHE astronomy (*S11, S12, S13*). The BDT method uses various parameters as input for the classification. Four parameters are of the classical Hillas-type (*S14*), where the measured width and length of a shower image is compared to the expectation for Monte-Carlo γ-rays and hadronic cosmic rays (MRSW, MRSL, MRSWO, MRSLO (*S6*)). Additionally, the averaged spread in reconstructed energy between triggered telescopes ΔE / E and the depth of the shower maximum $X_{\max}$ are used as input parameters (*S6*). It returns a continuous variable classifying the event, with gamma-ray like events at one end of the range and cosmic-ray background like events at the other end. Monte Carlo simulations of gamma rays and hadronic cosmic rays from observations without any gamma-ray emitter in the field-of-view were used to teach the BDT the differences between the two. After the training of the BDT, it was used to classify events of the NGC 253 observations. Thus, the hadronic background in the data set could be reduced by a factor of 2 compared to the H.E.S.S. standard analysis (*S3*), giving a 1.5 times higher significance and facilitating the detection of NGC 253 in VHE gamma-rays.

Using the BDT method, an excess of 283 (compared to 247 for the Model analysis) gamma rays above the threshold of 260 GeV is obtained, corresponding to a statistical significance of 4.9 σ (compared to 5.2 σ for the Model analysis). The flux value derived using this method is $F(> 260\,\mathrm{GeV}) = (5.7 \pm 1.3_{\mathrm{stat}} \pm 2.8_{\mathrm{sys}}) \times 10^{-13}\mathrm{cm}^{-2}\,\mathrm{s}^{-1}$ and confirms the value of the "Model analysis". In order to perform the comparison, one needs to extrapolate the BDT value to 220 GeV – the threshold of the "Model analysis." The extrapolated values are 6.8×10^{-13} $\mathrm{cm}^{-2}\,\mathrm{s}^{-1}$ and 7.3×10^{-13} $\mathrm{cm}^{-2}\,\mathrm{s}^{-1}$, respectively, assuming a power law with a spectral index of 2.1 and 2.5, respectively. These two indices are considered to encompass a realistic range of values. Both extrapolated flux values are well within the errors of the "Model analysis" result ($(5.5 \pm 1.0_{\mathrm{stat}} \pm 2.8_{\mathrm{sys}}) \times 10^{-13}$ $\mathrm{cm}^{-2}\,\mathrm{s}^{-1}$). The excess map is shown in Fig. S1 and the distribution of arrival directions of gamma rays around NGC 253 is depicted in Fig. S2. The agreement between Monte Carlo simulations and real data is shown for the methods in Fig. S4 and Fig. S5.

H.E.S.S. standard analysis

The H.E.S.S. standard analysis is based on a simple parametrization of the shower images by the Hillas parameters – width and length. These parameters are scaled to their nominal values for gamma rays and averaged over all the images of a given shower. The scaled parameters are subsequently used for event selection by means of cuts on these parameters and for reconstruction of physical properties of the shower (*S3*). However, the technique does not fully exploit the information obtained by the finely-pixellated cameras of modern IACT telescopes. Techniques which use the full pixel information – such as the Model analysis – and which include additional parameters and better account for correlations between the parameters – such as the BDT analysis – provide an improved background rejection and are more appropriate for analyzing the weakest sources. Using the standard analysis with standard background rejection cuts and

the reflected background estimation (*S3*), an excess of 252 gamma rays is found, resulting in a statistical significance of 3.2σ. This is in agreement with the expectations for a flux level of 0.3% of the Crab Nebula.

Systematic uncertainties

The flux determination is influenced by several sources of systematic uncertainties. The most important ones are uncertainties due to the atmospheric model used for Monte Carlo simulation ($\sim$20%), run-by-run variability and calibration ($\sim$20%), malfunctioning camera pixels ($\sim$10%), background estimation ($\sim$15%) and selection cuts ($\sim$15%). Additionally, the integral flux above a threshold can be biased by the energy-scale uncertainty of $\sim$15%. The total error of the flux above a threshold is thus very conservatively estimated as 40-50%.

The only systematic factor that can affect the detection significance is the uncertainty in background estimation, caused by a possible non-uniformity of the background over the field-of-view (FOV). In order to investigate this effect, a distribution of significances in off-source bins in the FOV is shown in Fig. S3. In case of a uniform background, this distribution will be Gaussian-distributed with mean of 0 and RMS of 1. The distribution in case of NGC 253 is well fit by a Gaussian of mean 0.1 and RMS of 1.1 (Fig. S3). The systematic error of the detection significance is constrained to approximately 10%. Note that using an alternative background estimation with ring-shaped control regions (*S3*) results in a higher significance of 5.9 σ (Model analysis) and 5.3 σ (BDT analysis). The more conservative values were thus used in deriving the results.

Cosmic ray transport in NGC 253

Three distinct processes can lead to losses of cosmic-rays in the nucleus of NGC 253. Inelastic collisions of hadronic cosmic-rays with protons and nuclei of the thermal gas lead to pion production. In addition to that cosmic-rays can also leave the starburst region convectively and diffusively. The timescale of the convective transport of cosmic rays out of the starburst region is $H/v \sim 10^5$ yr, where, for a distance of 2.6 Mpc, $H \sim 60$ pc is the height of the roughly cylindrical starburst region whose diameter is about 300 pc (*S15*), and $v \sim 500$ km/s is the assumed mean wind speed. The time between inelastic collisions of the hadronic cosmic rays and the protons and nuclei of the thermal gas at $E_{\rm p} \approx 1300$ GeV is also of the order of $10^5\,{\rm yr}$ for a mean gas density of about 600 protons ${\rm cm}^{-3}$. In addition the particles can also diffuse through the gas, being scattered by irregularities of the magnetic field. This latter process depends on the particle energy, with large uncertainties, but certainly increases with particle energy (*S16, S17*).

The detailed description of the interaction of cosmic rays with the gas is somewhat more complex than outlined above: the hot and rarefied gas produced by individual supernovae creates a contiguous hot gas component which pushes its way out from the starburst region between the massive clouds of cold gas from which the stars form. A high temperature ($10^6 - 10^7$ K) outflow is observed well beyond the starburst region (*S18*). Cosmic rays are accelerated in

shock waves that also produce the hot gas. Low energy particles are largely confined in this rarefied gas which tends to carry them out of the starburst region. Such a confinement is not likely for the high energy particles relevant for high-energy gamma-ray production. Hence they will also penetrate the dense cold gas surrounding the hot gas flow. For low energy particles this penetration is an open question. Cosmic-ray electrons will in any case lose a major fraction of their energy by Bremsstrahlung, IC collisions in the strongly enhanced radiation field and by synchrotron radiation in the magnetic field of the starburst region.

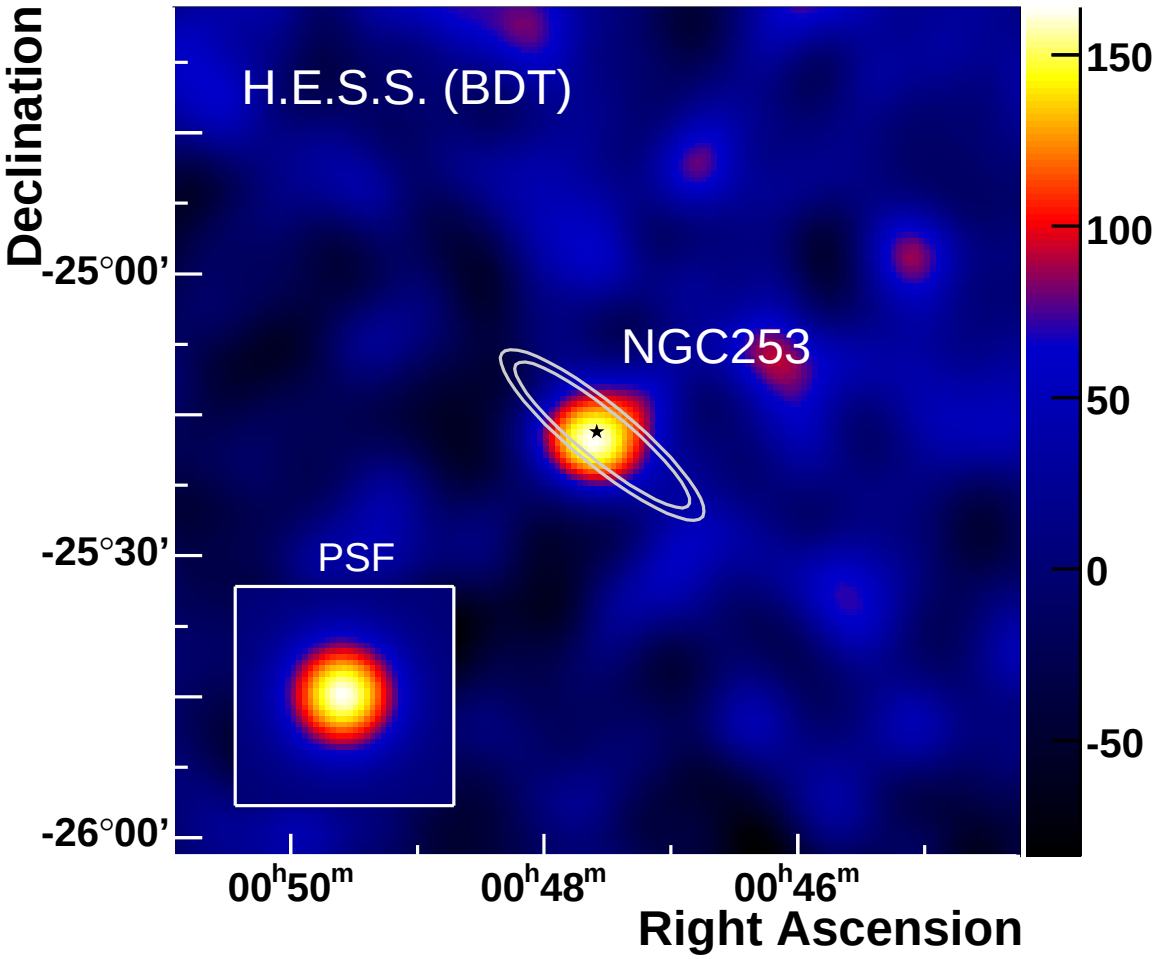

Fig. S1. A smoothed map of VHE gamma-ray excess of the $1.5^\circ \times 1.5^\circ$ region around NGC 253 obtained using the BDT method. A Gaussian with RMS of $4.2'$ is used to smooth the map in order to reduce the effect of fluctuations. The inlay represents an image of a Monte Carlo simulated point source (i.e. the point spread function of the instrument). The white contours correspond to constant optical surface brightness of 25 mag. arcsec.$^{-2}$ and 23.94 mag. arcsec.$^{-2}$ as given by fits of (*S19*).

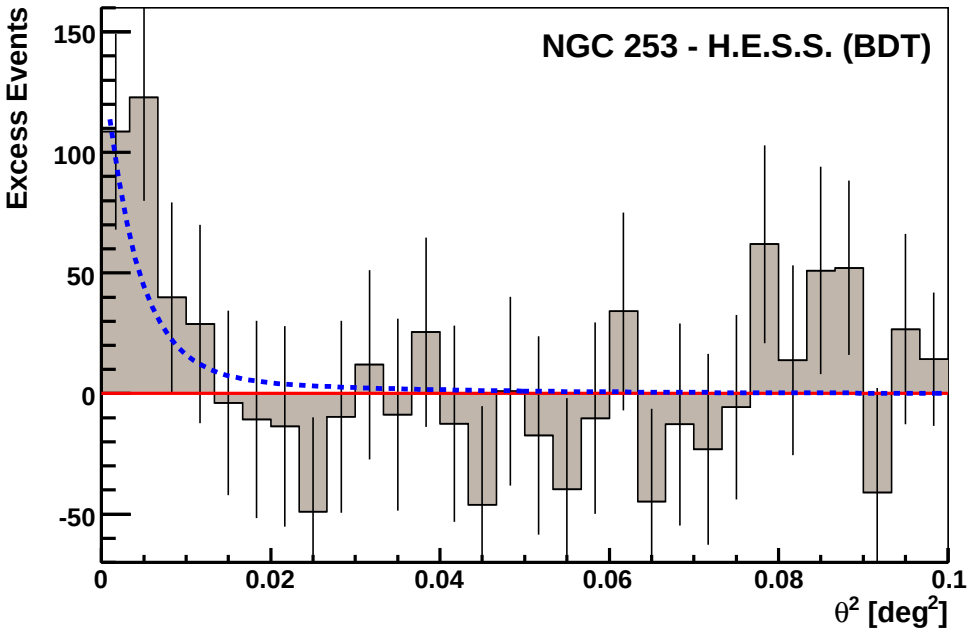

Fig. S2. Reconstructed directions of the gamma-ray like events around NGC 253 using the BDT method. θ denotes the angular distance between the arrival direction and the position of the object. The signal is consistent with a H.E.S.S. point source (the dashed blue line shows how H.E.S.S. sees a Monte-Carlo simulated point source using the BDT method). The background was estimated from off source regions, is uniform in the θ^2 representation and has been subtracted here.

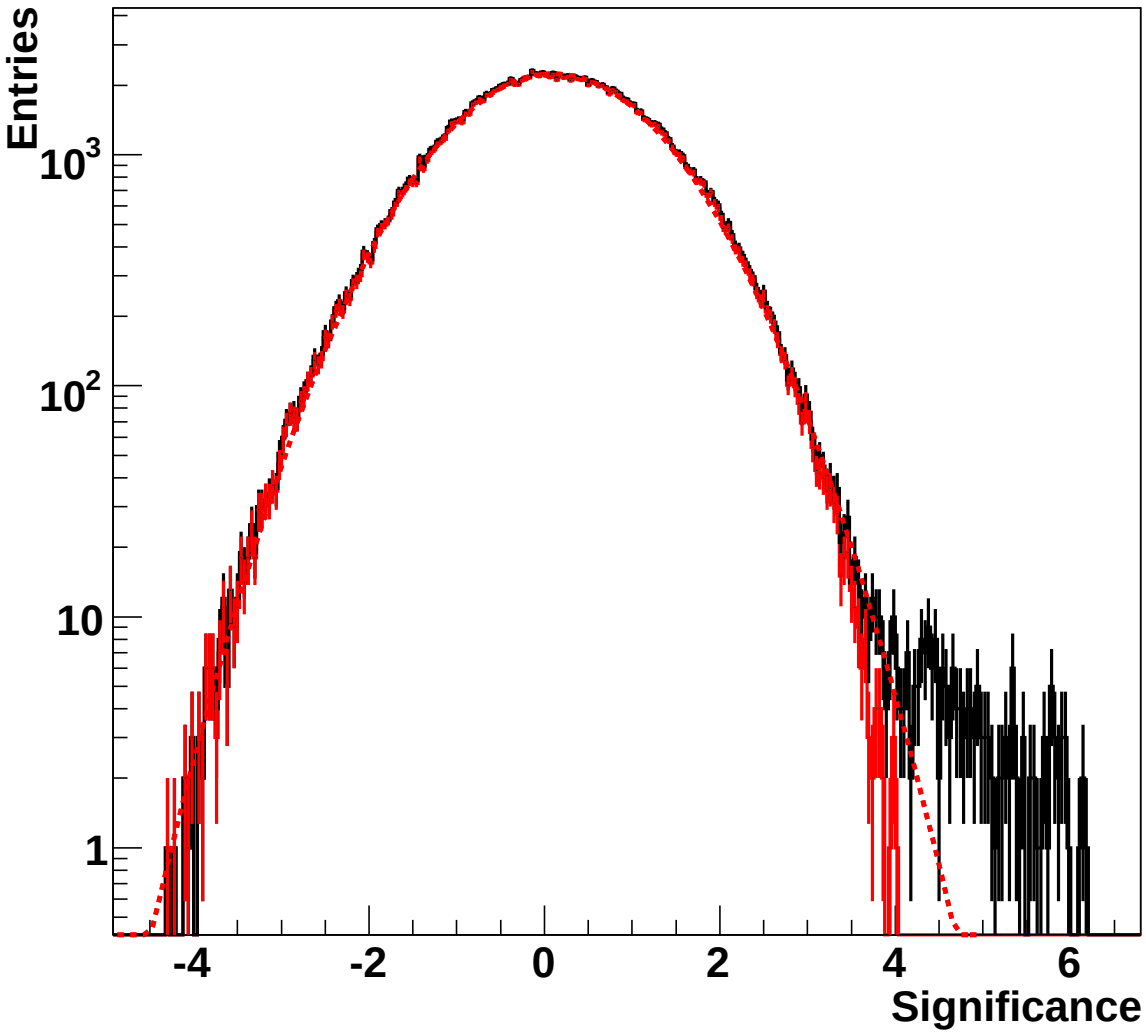

Fig. S3. Distribution of bin significances of the field-of-view including and excluding NGC 253 (black and red line, respectively) for the "Model analysis." The distribution excluding the source is fitted by a Gaussian with a mean of 0.1 and an RMS of 1.1 (red dashed line).

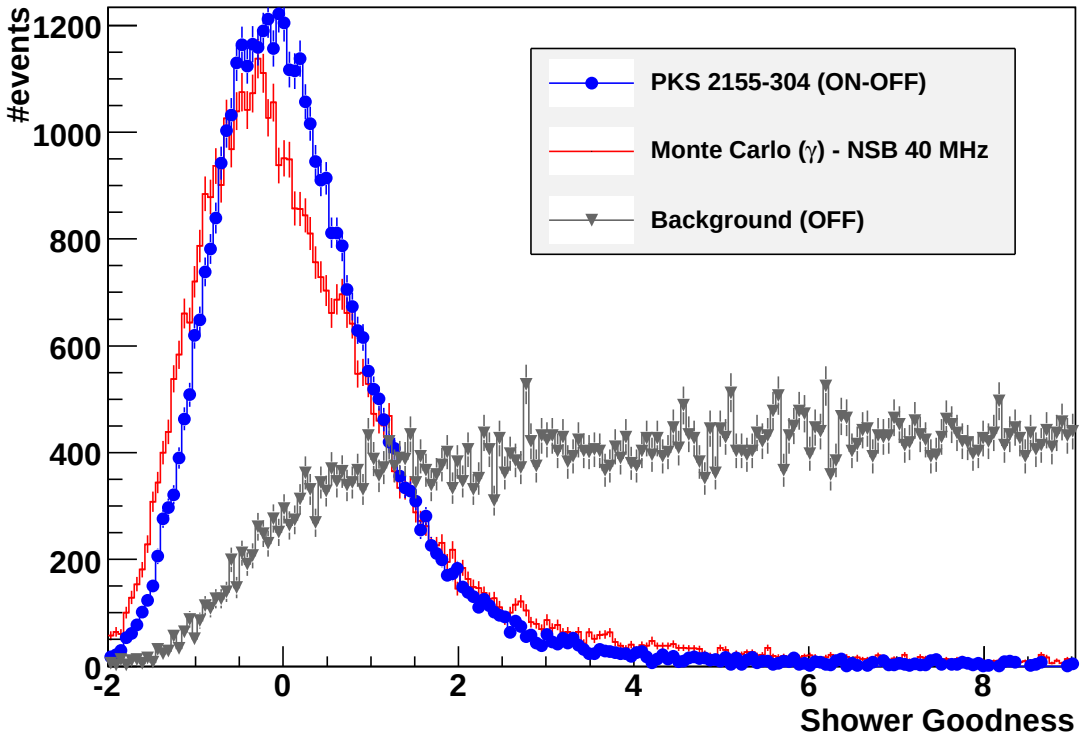

Fig. S4. Distribution of Shower Goodness for observational data taken on the blazar PKS 2155–304 (blue points indicate gamma-ray excess events, grey triangles cosmic-ray background events), compared with a simulation (red histogram) with a similar night sky background level. Figure taken from (*S4*).

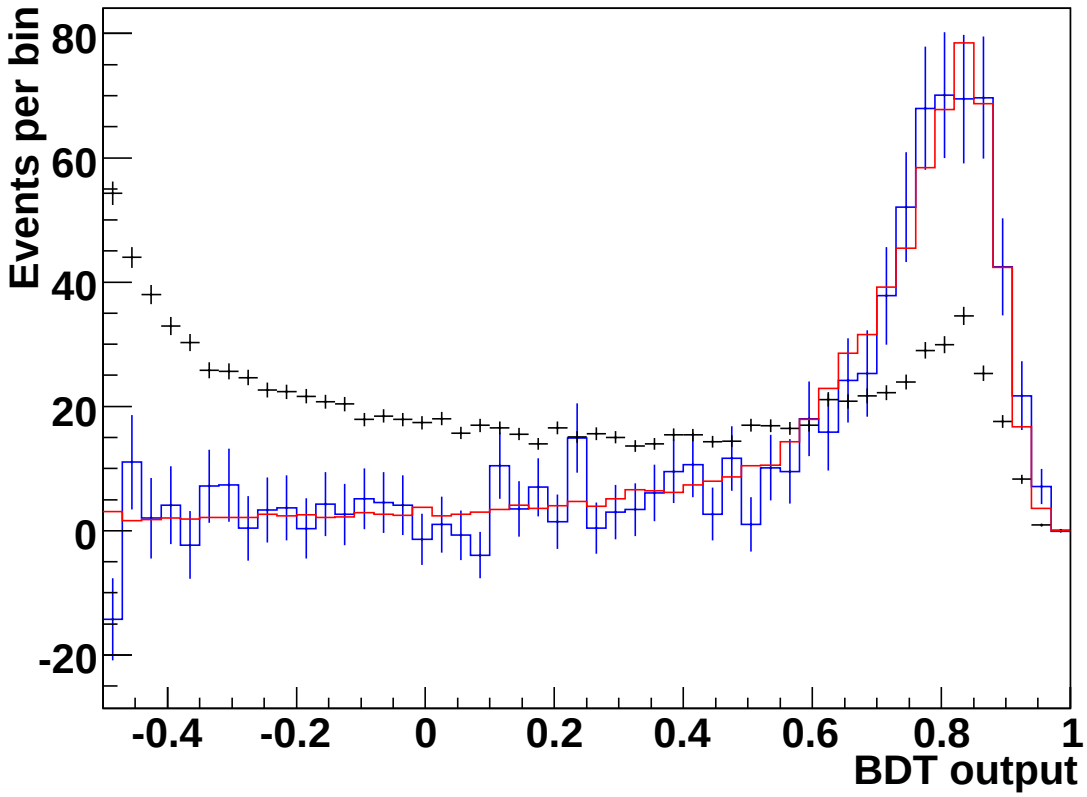

Fig. S5. Distribution of BDT output for observational data taken on the H.E.S.S. source HESS J1745–290 (blue points indicate gamma-ray excess events, grey points cosmic-ray background events), compared with a simulation (red histogram). Figure adapted from (*S6*).

References and Notes

S1. Hinton, J. A., *New Astronomy Review*, **48**, 331-337 (2004)

S2. Völk, H. J., & Bernlöhr, K., *Experimental Astronomy*, 12 (2009)

S3. Aharonian, F. *et al. (H.E.S.S. Collaboration), Astron. Astrophys.*, **457**, 899 (2006)

S4. de Naurois, M., Rolland, L., *Astroparticle Physics,* accepted for publication, (available at http://arXiv.org/abs/0907.2610)

S5. Breiman, L., Friedman, J., Stone, C.J., and Olshen, R.A., *Classification and Regression Trees* (Wadsworth, Stamford, 1984)

S6. Ohm, S., van Eldik, C., & Egberts, K., *Astroparticle Physics*, **31**, 383-391 (2009)

S7. Yang, H.-J., Roe, B.P. and Zhu, J., *Nucl. Instrum. Methods Phys. Res.*, **A 555**, 370 (2005)

S8. Abazov, V. M. *et al. (D0 Collaboration)*, Phys. Rev. D, **78**, 012005 (2008)

S9. Bailey, S., Aragon, C., Romano, R., *et al.*, *Astrophys. J.*, **665**, 1246 (2007)

S10. Breiman, L., *Machine Learning*, **45**, 1 (2001)

S11. Bock, R.K., Chilingarian, A., Gaug, M., *et al.*, *Nucl. Instrum. Methods*, **A 516**, 511 (2004)

S12. Albert, J., *et al. (MAGIC Collaboration)*, *Nucl. Instrum. Methods*, **A 588**, 424 (2008)

S13. Egberts, K. and Hinton, J.A. *(H.E.S.S. Collaboration), Advances in Space Research*, **42**, 473F (2008)

S14. Hillas, A. M. *Proc. 19th International Cosmic Ray Conference*, **3**, 445 (1985)

S15. Weaver, K. A., Heckman, T. M., Strickland, D. K., & Dahlem, M., *Astrophys. J.*, **576**, L19 (2002)

S16. Blandford, R. D. and Ostriker, J. P. *Astrophys. J.*, **349**, 625 (1980)

S17. Aharonian, F. *et al. (H.E.S.S. Collaboration), Astron. Astrophys.*, **442**, 177 (2005)

S18. Bauer, M., Pietsch, W., Trinchieri, G. *et al.*, *Astron. Astrophys.*, **489**, 1029 (2008)

S19. Pence, W. D., *Astrophys. J.*, **239**, 54 (1980)

Full list of authors

F. Acero[15], F. Aharonian[1,13], A.G. Akhperjanian[2], G. Anton[16], U. Barres de Almeida[8†], A.R. Bazer-Bachi[3], Y. Becherini[12], B. Behera[14], K. Bernlöhr[1,5], A. Bochow[1], C. Boisson[6], J. Bolmont[19], V. Borrel[3], J. Brucker[16], F. Brun[19], P. Brun[7], R. Bühler[1], T. Bulik[29], I. Büsching[9], T. Boutelier[17], P.M. Chadwick[8], A. Charbonnier[19], R.C.G. Chaves[1], A. Cheesebrough[8], L.-M. Chounet[10], A.C. Clapson[1], G. Coignet[11], M. Dalton[5], M.K. Daniel[8], I.D. Davids[22,9], B. Degrange[10], C. Deil[1], H.J. Dickinson[8], A. Djannati-Ataï[12], W. Domainko[1], L.O'C. Drury[13], F. Dubois[11], G. Dubus[17], J. Dyks[24], M. Dyrda[28], K. Egberts[1], D. Emmanoulopoulos[14], P. Espigat[12], C. Farnier[15], S. Fegan[10], F. Feinstein[15], A. Fiasson[11], A. Förster[1], G. Fontaine[10], M. Füßling[5], S. Gabici[13], Y.A. Gallant[15], L. Gérard[12], D. Gerbig[21], B. Giebels[10], J.F. Glicenstein[7], B. Glück[16], P. Goret[7], D. Göring[16], D. Hauser[14], M. Hauser[14], S. Heinz[16], G. Heinzelmann[4], G. Henri[17], G. Hermann[1], J.A. Hinton[25], A. Hoffmann[18], W. Hofmann[1], P. Hofverberg[1], S. Hoppe[1], D. Horns[4], A. Jacholkowska[19], O.C. de Jager[9], C. Jahn[16], I. Jung[16], K. Katarzyński[27], U. Katz[16], S. Kaufmann[14], M. Kerschhaggl[5], D. Khangulyan[1], B. Khélifi[10], D. Keogh[8], D. Klochkov[18], W. Kluźniak[24], T. Kneiske[4], Nu. Komin[7], K. Kosack[1], R. Kossakowski[11], G. Lamanna[11], J.-P. Lenain[6], T. Lohse[5], V. Marandon[12], O. Martineau-Huynh[19], A. Marcowith[15], J. Masbou[11], D. Maurin[19], T.J.L. McComb[8], M.C. Medina[6], J. Méhault[15], R. Moderski[24], E. Moulin[7], M. Naumann-Godo[10], M. de Naurois[19], D. Nedbal[20*], D. Nekrassov[1], B. Nicholas[26], J. Niemiec[28], S.J. Nolan[8], S. Ohm[1], J-F. Olive[3], E. de Oña Wilhelmi[1], K.J. Orford[8], M. Ostrowski[23], M. Panter[1], M. Paz Arribas[5], G. Pedaletti[14], G. Pelletier[17], P.-O. Petrucci[17], S. Pita[12], G. Pühlhofer[18,14], M. Punch[12], A. Quirrenbach[14], B.C. Raubenheimer[9], M. Raue[1,30], S.M. Rayner[8], O. Reimer[31,32], M. Renaud[12,1], F. Rieger[1,30], J. Ripken[4], L. Rob[20], S. Rosier-Lees[11], G. Rowell[26], B. Rudak[24], C.B. Rulten[8], J. Ruppel[21], V. Sahakian[2], A. Santangelo[18], R. Schlickeiser[21], F.M. Schöck[16], U. Schwanke[5], S. Schwarzburg [18], S. Schwemmer[14], A. Shalchi[21], M. Sikora[24], J.L. Skilton[25], H. Sol[6], Ł. Stawarz[23], R. Steenkamp[22], C. Stegmann[16], F. Stinzing[16], G. Superina[10], A. Szostek[23,17], P.H. Tam[14], J.-P. Tavernet[19], R. Terrier[12], O. Tibolla[1], M. Tluczykont[4], C. van Eldik[1], G. Vasileiadis[15], C. Venter[9], L. Venter[6], J.P. Vialle[11], P. Vincent[19], M. Vivier[7], H.J. Völk[1], F. Volpe[1], S.J. Wagner[14], M. Ward[8], A.A. Zdziarski[24], A. Zech[6]

1. Max-Planck-Institut für Kernphysik, P.O. Box 103980, D 69029 Heidelberg, Germany
2. Yerevan Physics Institute, 2 Alikhanian Brothers St., 375036 Yerevan, Armenia
3. Centre d'Etude Spatiale des Rayonnements, CNRS/UPS, 9 av. du Colonel Roche, BP 4346, F-31029 Toulouse Cedex 4, France

4. Universität Hamburg, Institut für Experimentalphysik, Luruper Chaussee 149, D 22761 Hamburg, Germany
5. Institut für Physik, Humboldt-Universität zu Berlin, Newtonstr. 15, D 12489 Berlin, Germany
6. LUTH, Observatoire de Paris, CNRS, Université Paris Diderot, 5 Place Jules Janssen, 92190 Meudon, France
7. IRFU/DSM/CEA, CE Saclay, F-91191 Gif-sur-Yvette, Cedex, France
8. University of Durham, Department of Physics, South Road, Durham DH1 3LE, U.K.
9. Unit for Space Physics, North-West University, Potchefstroom 2520, South Africa
10. Laboratoire Leprince-Ringuet, Ecole Polytechnique, CNRS/IN2P3, F-91128 Palaiseau, France
11. Laboratoire d'Annecy-le-Vieux de Physique des Particules, Université de Savoie, CNRS/IN2P3, F-74941 Annecy-le-Vieux, France
12. Astroparticule et Cosmologie (APC), CNRS, Universite Paris 7 Denis Diderot, 10, rue Alice Domon et Leonie Duquet, F-75205 Paris Cedex 13, France ‡
13. Dublin Institute for Advanced Studies, 5 Merrion Square, Dublin 2, Ireland
14. Landessternwarte, Universität Heidelberg, Königstuhl, D 69117 Heidelberg, Germany
15. Laboratoire de Physique Théorique et Astroparticules, Université Montpellier 2, CNRS/IN2P3, CC 70, Place Eugène Bataillon, F-34095 Montpellier Cedex 5, France
16. Universität Erlangen-Nürnberg, Physikalisches Institut, Erwin-Rommel-Str. 1, D 91058 Erlangen, Germany
17. Laboratoire d'Astrophysique de Grenoble, INSU/CNRS, Université Joseph Fourier, BP 53, F-38041 Grenoble Cedex 9, France
18. Institut für Astronomie und Astrophysik, Universität Tübingen, Sand 1, D 72076 Tübingen, Germany
19. LPNHE, Université Pierre et Marie Curie Paris 6, Université Denis Diderot Paris 7, CNRS/IN2P3, 4 Place Jussieu, F-75252, Paris Cedex 5, France
20. Charles University, Faculty of Mathematics and Physics, Institute of Particle and Nuclear Physics, V Holešovičkách 2, 180 00
21. Institut für Theoretische Physik, Lehrstuhl IV: Weltraum und Astrophysik, Ruhr-Universität Bochum, D 44780 Bochum, Germany
22. University of Namibia, Private Bag 13301, Windhoek, Namibia
23. Obserwatorium Astronomiczne, Uniwersytet Jagielloński, ul. Orla 171, 30-244 Kraków, Poland
24. Nicolaus Copernicus Astronomical Center, ul. Bartycka 18, 00-716 Warsaw, Poland
25. School of Physics & Astronomy, University of Leeds, Leeds LS2 9JT, UK
26. School of Chemistry & Physics, University of Adelaide, Adelaide 5005, Australia
27. Toruń Centre for Astronomy, Nicolaus Copernicus University, ul. Gagarina 11, 87-100 Toruń, Poland
28. Instytut Fizyki Jądrowej PAN, ul. Radzikowskiego 152, 31-342 Kraków, Poland
29. Astronomical Observatory, The University of Warsaw, Al. Ujazdowskie 4, 00-478 Warsaw, Poland
30. European Associated Laboratory for Gamma-Ray Astronomy, jointly supported by CNRS and MPG
31. Institut fr Astro und Teilchenphysik, Leopold-Franzens-Universitt Innsbruck, A6020 Innsbruck, Austria

32. KIPAC, Stanford University, Stanford, CA 94305, USA

† supported by CAPES Foundation, Ministry of Education of Brazil

‡ UMR 7164 (CNRS, Université Paris VII, CEA, Observatoire de Paris)